Mechanical Systems and Signal Processing 192 (2023) 110216

Contents lists available at ScienceDirect

Mechanical Systems and Signal Processing

journal homepage: www.elsevier.com/locate/ymssp

A transfer learning approach for acoustic emission zonal localization on steel plate-like structure using numerical simulation and unsupervised domain adaptation

Li Ai [a], Bin Zhang [b], Paul Ziehl [a,c,*]

[a] Department of Civil and Environmental Engineering, University of South Carolina, Columbia, SC, USA
[b] Department of Electrical Engineering, University of South Carolina, Columbia, SC, USA
[c] Department of Mechanical Engineering, University of South Carolina, Columbia, SC, USA

ARTICLE INFO

Keywords:
Acoustic emission
Finite element modeling
Source localization
Transfer learning
Unsupervised domain adaptation
Manifold embedded distribution alignment

ABSTRACT

The detection and localization of damage in metallic structures using acoustic emission (AE) monitoring and artificial intelligence technology such as deep learning has been widely studied. However, a current challenge of this approach is the difficulty of obtaining sufficient labeled historical AE signals for the training process of deep learning models. This problem can be approached through the implementation of transfer learning. The innovation of this paper lies in the development of a transfer learning approach for AE source localization on a stainless-steel structure when no historical labeled AE signals are available for training. A finite element model is developed to generate numerical AE signals for the training. Unsupervised domain adaptation (UDA) technology is utilized to reduce the distribution difference between the numerical and the realistic AE signals and to derive the localization results of the unlabeled realistic AE signals. The results suggest that the proposed approach is capable of localizing AE signals with high accuracy in the absence of labeled training data.

1. Introduction

Metallic materials are commonly utilized for infrastructure components. Some metallic structures such as rails, bridges, pipelines, and nuclear facilities are subject to structural damage due to environmental erosion [1–3], fatigue damage [4], and other factors after extended periods of use. Ensuring the integrity and safety operation of metallic structures over their service life is a significant task. Traditional approaches including intermittent visual inspection have been applied to inspect and monitor damage in metallic structures. However, visual inspection of large-scale structures is usually time-consuming and prone to human error. To improve the reliability and efficiency of damage inspection, an automated monitoring approach is highly desirable.

Acoustic emission (AE) is a structural health monitoring (SHM) method that is extremely sensitive to damage propagation in materials [5]. The detection and localization of cracks in metallic structures can be implemented by deploying an AE sensor array [6–8]. Pearson et al. [6] developed the Akaike information criteria Delta-t mapping technique to overcome the difficulty of applying traditional time-of-arrival techniques to locate AE events in complex metal structures. The results show that the Akaike information criteria Delta-t mapping technique is a feasible option for AE source localization. Sai et al. [7] proposed a novel AE localization method

* Corresponding author.
E-mail addresses: ail@email.sc.edu (L. Ai), zhangbin@cec.sc.edu (B. Zhang), ziehl@cec.sc.edu (P. Ziehl).

https://doi.org/10.1016/j.ymssp.2023.110216
Received 24 July 2022; Received in revised form 9 January 2023; Accepted 13 February 2023
Available online 24 February 2023

and a detection system for AE localization based on time reversal focusing imaging and a fiber Bragg grating sensor network. Results indicate the method improved AE detection and source localization with high precision. Yan et al. [8] proposed a new method to solve the multi-leakage source location problem of metal pressure vessels using AE sensors combined with a multi-signal classification (MUSIC) algorithm and wavelet packet analysis. AE sensors were deployed into a linear array to acquire signals from multiple leakage sources. The results suggested that the method can successfully locate two leak sources. Results from previous studies indicated that AE monitoring with multiple sensors has a good capability to detect and identify cracks in metallic specimens. However, challenges arise when applying AE monitoring in realistic metallic infrastructures. For some cases, the available area for sensor attachment is limited, and it would therefore be difficult to deploy sensor arrays to localize the damage. An intelligent and automated localization approach through the use of only a single AE sensor is desirable, and in many instances would be of benefit to the detection and localization of damage in metallic infrastructures.

Adopting and leveraging artificial intelligence techniques including machine learning and deep learning may be a promising approach. Machine learning generally refers to supervised intelligent data processing techniques [9]. By learning features extracted from the data, machine learning can understand the pattern of data and make a decision [10]. Machine learning models such as artificial neural network, support vector machine (SVM), K-nearest neighbor (KNN), and random forest have been widely utilized for signal processing [11–14]. Deep learning methods are improved intelligent techniques which are based on machine learning. These methods can automatically learn features from complex data sets [15]. The application of deep learning in SHM has been investigated in numerous studies [16–18]. In recent years, machine learning and deep learning have also been applied to AE localization using a single AE sensor. AE signals that are generated from different locations on a structure have different reverberation patterns [19–21]. Deep learning algorithms can be used to automatically learn the reverberation patterns from the entire length of waveforms and relate the patterns to the zone where the signal is generated [21–23]. Ebrahimkhanlou et al. [21] proposed a deep learning framework based on a stacked autoencoder network to locate AE events on metallic structures. A good localization accuracy was obtained by using the proposed framework. The results indicated that CNN has the potential to automatically identify reverberation patterns from the AE signals and to locate the damage to its corresponding zone precisely. Ai et al. [22] studied the single sensor AE source localization on the stainless steel canister. A stacked autoencoder network was utilized to analyze the entire waveforms of AE signals and conduct zonal source localization. Han et al. [23] localized the damage on an engine using one AE sensor. PLB was used to simulate the damages in different parts of the engine. The wavelet images produced by the full-length AE waveforms were used as the input of a CNN. The CNN models successfully estimate the damaged part that generates the AE signals.

Previous studies have proven that using deep learning to localize AE signals is promising. However, a current challenge of using the supervised learning algorithms on AE source localization is the difficulty with access to the labeled AE signals for existing structures. Transfer learning (TL) is a strategy to assist the supervised learning task when the available training data is limited [24]. TL has been utilized in the application of acoustic emission. Li et al. [25] utilized a multi-branch CNN model for AE wave classification on rails. The weights of a pre-trained AlexNet are adopted, except the last fully connected layer, to save time for training and to acquire a robust network using limited available AE training data. Chen et al. [26] proposed a transfer learning approach for AE–based rail condition evaluation. The weights of a CNN model trained by open-access audio data utilized the AE signals collected from the experiment. TL demonstrated good performance in the aforementioned studies. However, the limitations of the current study of using deep learning and transfer learning to localize AE signals is that those studies only focused on the scenarios when the realistic AE signals for training are limited but still available. In other words, a small amount of realistic historical AE signal is still an unavoidable necessity in those studies. To address the limitation, this research proposes a novel TL approach for AE localization on stainless steel structures. This approach does not need to be trained by any realistic AE signals collected in the real world. A finite element model is developed to generate numerical AE signals for the training of deep learning algorithms. Unsupervised domain adaptation (UDA) technology is utilized to decrease the difference between the generated numerical AE signals with realistic AE signals. The main contributions of this research are: (1) An novel TL approach without any labeled historical AE signals for training is firstly proposed for AE source localization by using numerical AE signals and a UDA technology named manifold embedded distribution alignment (MEDA); (2) A finite element model using six different excitation functions and a linear combinational output is designed to produce the numerical AE waveforms; (3) The impact of the iteration number and dimension of manifold space of MEDA has been illustrated; (4) The comparison of the localization performance between the TL approach without UDA technology and the proposed TL approaches using three different UDA technologies has been summarized and discussed;

The remainder of the paper is organized as follows: Section 2 briefly introduces the theoretical background of transfer learning and unsupervised domain adaptation. Section 3 presents the experimental setup, including the material of the specimen and the acoustic emission setup. The proposed TL approach for AE source localization, including the acoustic emission waveform simulation, is explained in Section 4. Section 5 discussed the performances of the proposed TL approach using different UDA methods. The conclusions are discussed in Section 6.

2. Theoretical background

2.1. Transfer learning and unsupervised domain adaptation

The basic principles of TL and unsupervised domain adaptation (UDA) are introduced in this section. Generally, a sufficient number of training data and the corresponding labels are required by a supervised learning model such as artificial neural network and decision tree. However, in some cases, adequate training data with labels is difficult to obtain. TL is a strategy to solve this problem. Assuming

there are two datasets. The first dataset is $\{X_s, Y_s\} = \{(x_{s1}, x_{s2}, \cdots, x_{sm}), (y_{s1}, y_{s2}, \cdots, y_{sm})\}$, where $(y_{s1}, y_{s2}, \cdots, y_{sm})$ is the label of $(x_{s1}, x_{s2}, \cdots, x_{sm})$, and is known. The second dataset is $\{X_t, Y_t\} = \{(x_{t1}, x_{t2}, \cdots, x_{tn}), (y_{t1}, y_{t2}, \cdots, y_{tn})\}$, with the label $(y_{t1}, y_{t2}, \cdots, y_{tn})$ being unknown. The concept of transfer learning is to execute the classification of $\{X_t, Y_t\}$ based on the acquired knowledge from the model with training on $\{X_s, Y_s\}$. The dataset $\{X_s, Y_s\}$ is referred to as the source domain (D_S) and the dataset $\{X_t, Y_t\}$ to be classified is referred to as the target domain (D_T). One of the issues of TL is, the performance of TL based on D_S and D_T is not good when the difference between the source domain and the target domain is significant. UDA is a technique to learn the domain invariant features from the annotated source domain and the unannotated target domain and to reduce the distribution difference [27].

2.2. Manifold embedded distribution alignment

As mentioned above, $D_S : \{X_s, Y_s\}$, and $D_T : \{X_t, Y_t\}$ have different data distribution which means they have different marginal probabilities ($P_s(x_s) \neq P_t(x_t)$) and different conditional probability ($Q_s(x_s|y_s) \neq Q_t(x_t|y_t)$). Manifold embedded distribution alignment (MEDA) is an UDA algorithm to reduce the distribution difference by utilizing manifold feature learning and dynamic distribution alignment [28]. Manifold feature learning is utilized to reduce the data drift between the source domain and the target domain. Dynamic distribution alignment is employed to align the marginal and conditional distributions. The MEDA aims to articulate a cross-domain classifier f to predict the unknown Y_t.

2.2.1. Manifold feature learning

Manifold feature learning is an UDA method [29]. Manifold refers to the space with local Euclidean spatial properties, including curves and surfaces of various dimensions. One of the characterizations of manifold space is that features in the manifold space usually have good geometric structure. The manifold learning leverages this characteristic to avoid feature distortions by mapping high-dimensional data into a low-dimensional manifold space. In MEDA, the geodesic flow kernel (GFK) is employed to conduct the manifold feature transformation. More details about GFK can be found in [30]. The process of manifold feature learning in MEDA is presented in Fig. 1.

2.2.2. Dynamic distribution alignment

The importance of marginal distributions (P) and conditional distributions (Q) of the source domain and target domain tend to vary with the similarity of the two domains. For instance, marginal distribution is more significant when there are large differences between the source domain and target domain, while conditional distribution is more dominant when the two domains have high similarities. Therefore, the importance of P and Q needs to be quantitatively measured, rather than simply counting them with the same weights. To accomplish this goal, the dynamic distribution alignment process is proposed in MEDA to dynamically evaluate the importance of these two distributions. The process of dynamic distribution alignment may be presented by Eq. (1):

$$\overline{D_f}(D_S, D_t) = (1-\omega) D_f(P_s, P_t) + \omega \sum_{c=1}^{C} D_f^{(t)}(Q_s, Q_t) \tag{1}$$

where, $c \in \{1, 2, 3, \cdots, C\}$ represents the classes of data, $\overline{D_f}(D_S, D_t)$ is the distribution after alignment, $D_f(P_s, P_t)$ refers to the marginal distribution alignment, $D_f^{(t)}(Q_s, Q_t)$ is the conditional distribution alignment for class t, and $\omega \in [0, 1]$ refers to the adaptive factor. If ω is close to 0, this is an indication that the distribution difference between the source domain and target domain is large. Therefore,

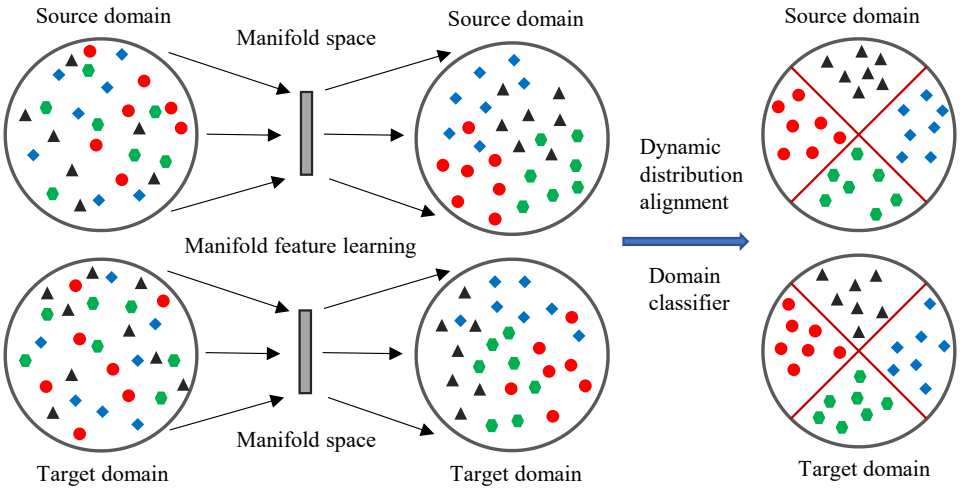

Fig. 1. Procedures of MEDA.

marginal distribution alignment is more important. If ω is close to 1, this indicates that the difference between domains is small, and the conditional distribution alignment is more dominant. If $\omega = 0.5$, it means the marginal and conditional distribution share equal importance. The optimizing of ω will be introduced in the following paragraph.

Maximum mean discrepancy (MMD) is utilized to explore the distribution distance between two domains [31]. The MMD distance between domain a and b may be obtained by Eq. (2):

$$MMD^2(a,b) = \|E_m[\theta(Z_s)] - E_c[\theta(Z_t)]\|^2_{H_k} \tag{2}$$

where, $MMD(a,b)$ is the distance between domain a and b, H_k refers to the reproducing kernel Hilbert space induced by feature map $\theta(\cdot)$, and $E[\cdot]$ is the mean of the embedded samples, m and c represent marginal and conditional distribution, respectively. Z_s and Z_t are the features transformed to the reproducing kernel Hilbert space.

For the purpose of computing the MMD about f, the projected MMD [32] is adopted to calculate the marginal distribution alignment ($D_f(P_s,P_t)$) and conditional distribution alignment ($D_f^{(t)}(Q_s,Q_t)$) by the following equations:

$$D_f(P_s,P_t) = \|E_m[f(Z_s)] - E_c[f(Z_t)]\|^2_{H_k} \tag{3}$$

$$D_f^{(t)}(Q_s,Q_t) = \|E_m[f(Z_s^{(t)})] - E_c[f(Z_t^{(t)})]\|^2_{H_k} \tag{4}$$

By substituting Eqs. (3) and (4) into Eq. (1), the final dynamic distribution alignment is obtained by Eq. (5):

$$\overline{D_f}(D_S,D_t) = (1-\omega)\|E_m[f(Z_s)] - E_c[f(Z_t)]\|^2_{H_k} + \omega\sum_{t=1}^{T}\|E_m[f(Z_s^{(t)})] - E_c[f(Z_t^{(t)})]\|^2_{H_k} \tag{5}$$

After the manifold feature learning and dynamic distribution alignment are completed, a domain classifier can be derived by Eq. (6). The procedure of dynamic distribution alignment and classification is illustrated in Fig. 1.

$$f = \operatorname{argmin}\sum_{i=1}^{t}(y_i - f(Z_i))^2 + \alpha\|f\|_K^2 + \beta\overline{D_f}(D_S,D_t) + \gamma R_f(D_S,D_t) \tag{6}$$

where, $R_f(\cdot)$ is a Laplacian regularization to utilize the similar geometric properties of the nearest point in the manifold, and α, β and γ are regularization parameters. $\|f\|_K^2$ denotes the squared norm of f.

The label Y_t of the target domain can be obtained by the domain classifier. However, the confidence level of the obtained label may not be high because the adaptive factor ω might not be the optimized value. Therefore, an optimization process of ω is designed in MEDA. The main procedure can be expressed by Eq. (7):

$$\omega = 1 - \frac{d_P}{d_P + \sum_{t=1}^{T} d_Q} \tag{7}$$

where d_P refers to the A-distance [33] of marginal distribution, and d_Q refers to the A-distance of the conditional distribution of each class.

The adaptive factor ω is calculated at every iteration of the dynamic distribution adaptation, and the predicted label Y_t is also updated with the iterations. More details about dynamic distribution alignment can be found in [28].

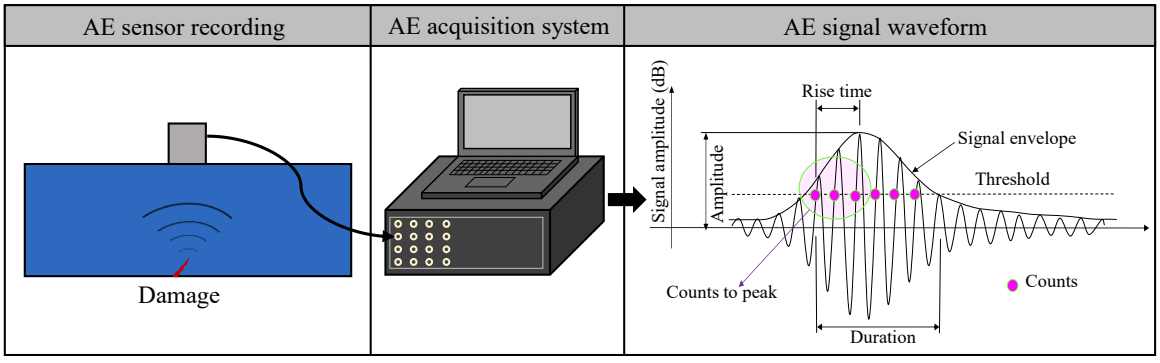

Fig. 2. Schematic of acoustic emission approach.

2.3. Acoustic emission monitoring

Acoustic emission is a physical phenomenon, which is related to the stress waves generated by the rapid release of elastic energy when cracks or damage form in materials [34]. AE waves can be detected and collected by deploying AE sensors on the surface of an object. An AE data acquisition system, including the sensors, is used to convert the stress waves into AE signals which are commonly recorded as a voltage. The method of recording and processing AE signals to diagnose the health status of an object is referred to as AE monitoring and evaluation [35]. The procedures of AE monitoring are illustrated in Fig. 2. Conventional approaches such as the time of arrival method have been widely utilized to localize AE sources by deploying sensor arrays. Usually, three or more sensors are needed. Several studies have focused on using one AE sensor to localize the AE source based on deep learning algorithms [21,22,36]. However, a current challenge of this approach is the difficulty of obtaining the labeled AE signals for the training process of machine learning and deep learning models. A TL approach is proposed in this paper to address this limitation. The implementation procedure of the approach is presented in Section 2.3. Details of the approach will be introduced in Section 4.

2.4. Implementation procedure of the proposed TL approach

The proposed TL approach consists of numerical modeling, data augmentation, transfer learning using manifold embedded distribution alignment, and conducting source localization on realistic AE signals. The detailed implementation steps are described as follows:

1) Develop a finite element model that has the same dimensions as the structure being monitored. Utilized the model to generate the numerical AE signals.
2) Perform data augmentation on the numerical AE signal dataset by adding Gaussian white noise.
3) Train a deep learning model using the augmented numerical AE signal dataset, while using manifold feature learning and dynamic distribution alignment to reduce the differences in marginal probabilities and conditional probabilities differences between the digital AE signal and the real AE signal.
4) Utilized the trained model to localize the realistic AE signals that are captured on the structure being monitored.

3. Materials and experimental setup

The experiment was conducted with the aim of collecting AE signals as the source domain for the TL AE source localization approach proposed in this paper (introduced in Section 4). A specimen fabricated from 304 stainless steel is utilized in the experiment. The dimension of the specimen is 0.61 × 0.30 × 0.00635 m. A plan view of the specimen is provided in Fig. 3.

3.1. Experimental procedure

The Hsu-Nielsen pencil lead break (PLB) is one of the most widely used artificial sources to generate AE signals by conducting pencil lead breaks on the object to which the AE sensor is attached [37]. In this paper, A Hsu-Nielsen PLB test was conducted to simulate the

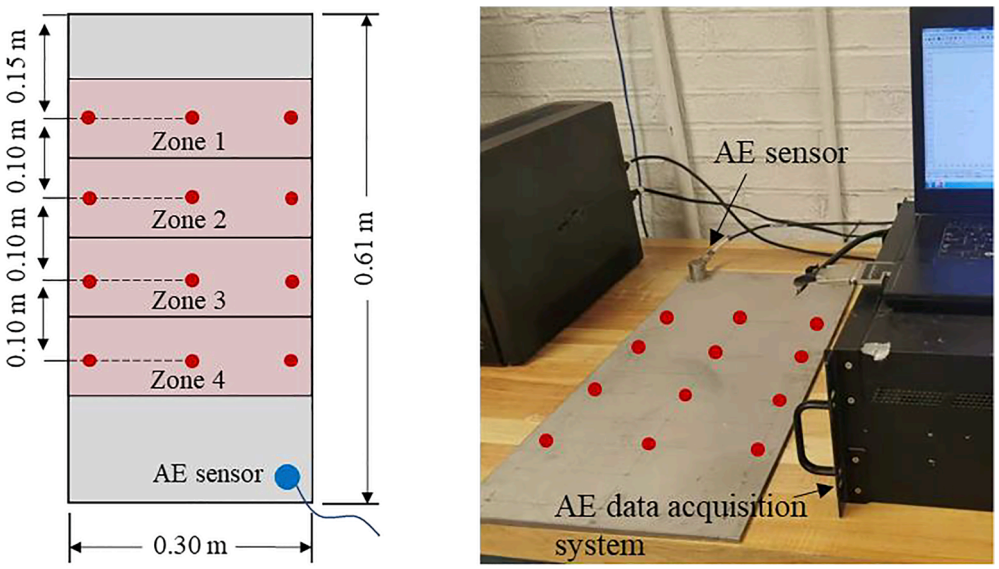

Fig. 3. Experimental setup.

cracks on the steel plate with an angle of 30°. Four zones were set up on the specimen. Using the signals from some points to represent the signals in an area is a simplified method used by previous studies [23,38–41]. In this paper, three points were marked with a red dot in each zone. The PLB was repeated 100 times on each of these points. A single AE sensor was attached to the corner of the specimen. In the experiment, 1200 AE events were collected. The location of the AE sensor and the locations for PLB in four zones are shown in Fig. 3.

3.2. Acoustic emission instrument setup

The hardware of the AE system was produced by the MISTRAS Group Inc., Princeton Junction, New Jersey. The AE sensor utilized in this experiment is a wideband type WDI-AST. The sensors have an operating frequency range of 100–900 kHz. The AE sensors were attached to the specimen by using red double/bubble epoxy, and AE signals were acquired by a 16-channel DISP system. The details regarding the AE acquisition parameters are presented in Table 1. The pre-trigger time, which recovers AE waveforms before the threshold crossing, was defined as 256 μs, the sampling rate was 1 M samples/s, and the duration was set to 2,000 μs. The peak definition time (PDT), which refers to the time between the first threshold crossing to the peak amplitude, was defined as 200 μs, and the hit definition time (HDT) was set to 400 μs. This controls the stop point of recording and is usually twice the peak definition time. The hit lockout time (HLT), which minimized the recording of late-arriving signals and reflected hits, was set to 400 μs. The threshold was 32 dB, and the high and low pass digital filters were set to 20 kHz, and 1 MHz, respectively.

4. The proposed TL approach for AE source localization

In this paper, the AE source localization is considered as a classification problem, with the AE signals classified to their corresponding zone. A TL approach for AE source localization by leveraging numerical simulation and UDA is proposed. This approach aims to localize the AE events using one AE sensor while no labeled training data is available. A three-dimensional finite element model is developed to simulate the generation of AE signals. The numerical AE signals obtained by the finite element model will be utilized for data augmentation to enable the large amount of data required for the following training process. The data after augmentation is utilized as the source domain. The AE signals collected during the experiment are employed as the target domain. An improved manifold embedded distribution alignment is utilized as the UDA method to reduce the difference between the source and the target domain, and to finally derive the source localization results. The workflow of the proposed approach is presented in Fig. 4.

4.1. Acoustic emission waveform simulation

The finite element model to simulate AE signals emitted is presented in this section. The model was developed in the commercial finite element platform ABAQUS, and the solver is Explicit. By applying the excitation source and reducing the size of the mesh, the high-frequency dynamic response may be obtained [42–46]. The finite element model has the same dimensions as the steel plate in the experiment. The material property utilized in the model is in agreement with the experimental specimens (304 stainless steel with the young's modulus 193 GPa, the density is 8000 kg/m^3). The mesh size is 0.001 m. The zonal definition and excitation points are kept the same with the experiment (Fig. 5a and 5b).

During the experiment, when conducting pencil lead breaks (PLBs) in one point, the locations to apply the excitations were not exactly in the same points; due to human error a slight position shift is inevitable. To simulate the position shift and also increase the diversity of numerical signals, five sub-points are designed in the model as shown in Fig. 5c. The excitation sources will be applied in the five sub-points to generate the numerical signals in one zone.

In previous studies, the PLB has been simulated by several excitation functions such as the cosine bell function [47], exponential function [48], and Gaussian distribution function [49]. For this study the cosine bell function is selected (Eq. (8)) and the exponential function (Eq. (9)) as the excitation source in the finite element model. The expressions of the excitation functions are presented as follow:

$$F(t) = \begin{cases} \frac{1}{2} - \cos\left((\pi t)\frac{1}{2T}\right) for t \le T \\ 1 for t > T \end{cases} \tag{8}$$

Table 1
AE acquisition parameters.

Setting	Value
Hit Definition Time	400 μs
Peak Definition Time	200 μs
Hit Lockout Time	200 μs
Sampling Rate	1 M samples/s
Threshold	32 dB
Pre-trigger Time	256 μs
High Pass Digital Filter	20 kHz
Low Pass Digital Filter	1 MHz

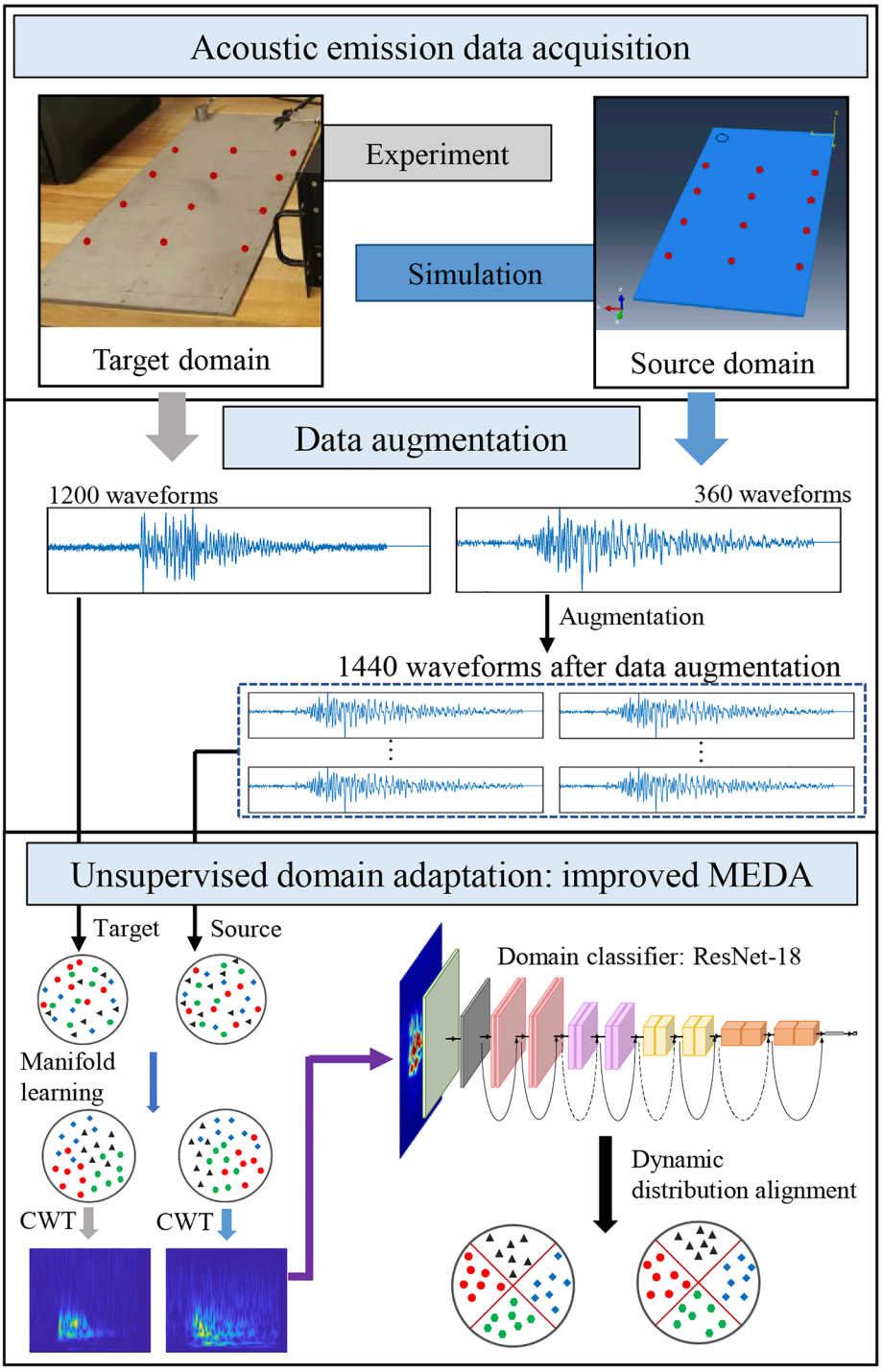

Fig. 4. Schematic of the proposed TL AE source localization approach.

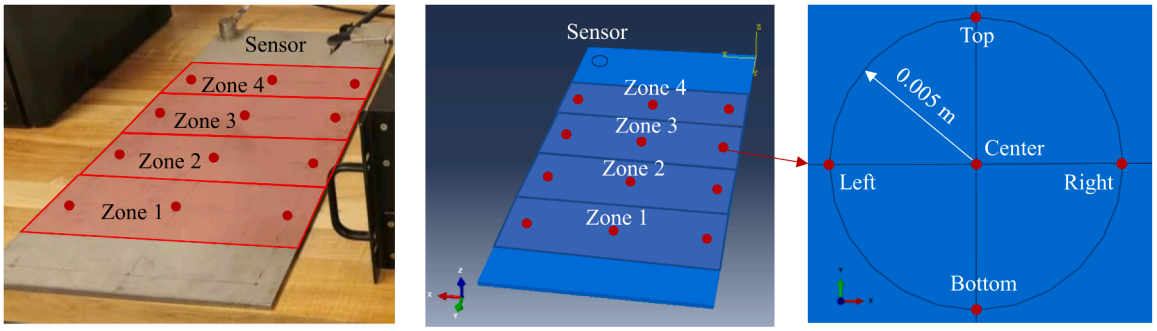

Fig. 5. Finite element setup: (a) experimental specimen; (b) finite element model; (c) excitation locations in zone 1.

$$F(t) = \begin{cases} \exp\left(-\left(\frac{1}{2}(t-T)\frac{5}{T}\right)^2\right) for t \le T \\ 1 for t > T \end{cases} \tag{9}$$

where T refers to the period of the functions. To further increase the diversity of the numerical signals and simulate the randomness of the period of PLB applied in the experiment, three different periods: $T_1 = 1\mu s$, $T_2 = 1.25\mu s$, and $T_3 = 1.5\mu s$ are utilized for the excitation functions. All six excitation sources implemented in the model are illustrated in Fig. 6.

The modeled PLB starts at a load of 0 N and ramps up to a certain value, after which it stays constant. The actual load of the PLB breaks during the experiment is unknown. Several previous literatures utilized 1 N as the assumption magnitude of PLB excitation [46–50]. This assumption value is of low significance because this value will only affect the amplitude of the obtained numerical waveform which will be normalized [48]. Therefore, this paper assumes the magnitude of the load is 1 N, and the acquired numerical waveform is normalized to −1 and 1.

When the stress wave passes through an AE sensor, the bottom surface of the AE sensor is excited by the stress wave and the signal is thereby generated and captured. However, in the FE model, the dynamic response can be obtained by extracting the relationship between displacement and time at a node of the model and filtering it through an anti-aliasing filter. This node has an infinitely small geometry that cannot represent the whole bottom surface of the sensor. Therefore, a combination of multiple nodes would be a strategy to simulate the AE bottom surface. In this paper, a single line output was employed [48]. The out-of-plane displacements of the nodes in a single straight line are collected. A weight is assigned to each node to account for the circular geometry of the sensor. Assuming the single line output is composed of n nodes, the combinational output of the n nodes can be calculated based on the following equations:

$$w_i = \frac{dy \bullet dx_i}{\sum_{i=1}^{n} dy \bullet dx_i} = \frac{dy \bullet \sqrt{\left(\frac{D}{2}\right)^2 - Cy_i^2}}{\sum_{i=1}^{n} dy \bullet \sqrt{\left(\frac{D}{2}\right)^2 - Cy_i^2}} \tag{10}$$

$$U_{sensor} = \sum_{i=1}^{n} w_i \bullet U_i \tag{11}$$

where w_i is refers to the weight that assigns to the *ith* node from the left side in the x-direction, dy refers to the distance between two nodes, D is the diameter of the AE sensor, and Cy_i refers to the distance from the *ith* node to the center of the circle, U_{sensor} is the single line output of the sensor and U_i is nodal out-of-plane displacement of the *ith* node. All the parameters in the equation are shown in the

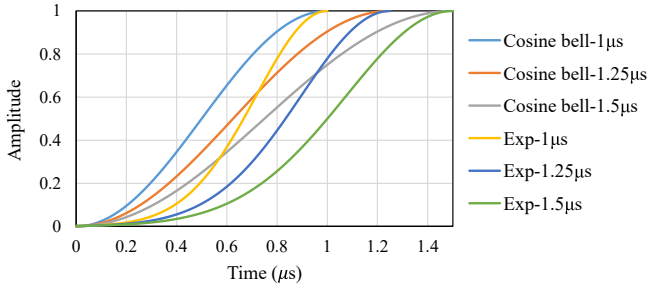

Fig. 6. Excitation functions.

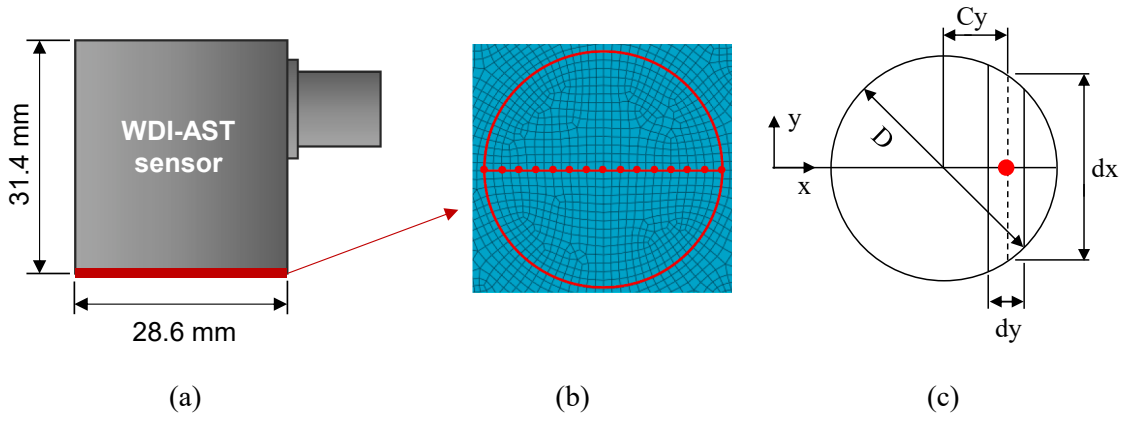

Fig. 7. Numerical waveform output setting: (a) geometric dimension of WDI-AST sensor; (b) nodes definition for single line output in FE model; (c) parameters to calculate single line output.

schematic bottom view of the sensor (Fig. 7c).

The location of the sensor in the finite element model is the same as in the experiment shown in Fig. 5a and 5b. The geometric dimensions of the WDI-AST sensor are shown in Fig. 7a. The diameter of the bottom surface is 28.6 mm. The single line output defined in the FE model is presented in Fig. 7b. Fifteen nodes can be observed on the line.

AE sensors convert the excitation on the bottom to the electrical signal through the piezoelectric material. Different types of AE sensors have various frequency sensitive ranges because their piezoelectric material properties are not the same. The stable sensitive frequency range of the WDI-AST sensor is from 100 to 900 kHz. A band pass filter can be applied to simulate the frequency response of the WDI-AST sensor. Butterworth filter is a widely used digital filter which has high pass, low pass, band pass, band reject and other types [51–53]. It has been utilized to process the AE signals [53–55], and simulate the frequency response of AE sensor in previous study [48]. Therefore, in this paper, a bandpass Butterworth filter with the frequency of 100–900 kHz is developed and used to filter the U_{sensor} obtained from the finite element model. The filtered waveforms are the final numerical AE waveforms.

In summary, four zones are defined in the finite element model, while each zone has five sub-points. The six excitation sources are implemented in each of the sub-points. In total, 120 numerical AE waveforms can be obtained after the simulation is completed.

4.2. Data augmentation of numerical waveforms

One challenge for simulations of the acoustic emission phenomena is the lengthy computing time required due to the very small mesh size. In this study, the average time for the finite element model to generate one numerical signal is 26 min conducted on a workstation with a CPU-Intel i7-4970 3.40 GHz, 32 GB RAM. One hundred and fifty-six hours were required to generate all 360 numerical AE signals. It is difficult to produce sufficient data for the source domain based on finite element simulations alone. A data augmentation process is therefore desirable to reduce the time to produce a sufficient amount of source domain data. A signal that has Gaussian white noise added to it will not be the same as the original signal but will have a high degree of similarity. Inspired by this, a data augmentation process is developed by adding Gaussian white noise to the original signals in the source domain. By changing the signal power of the noise, new datasets with slight differences can be derived. Four different signal powers 10, 15, 20, and 25 were employed to conduct the data augmentation. Finally, 1080 waveforms were obtained. The computing time for data augmentation is 0.27 s. These waveforms are prepared as the source domain for the improved MEDA (introduced in Section 4.3). It should be

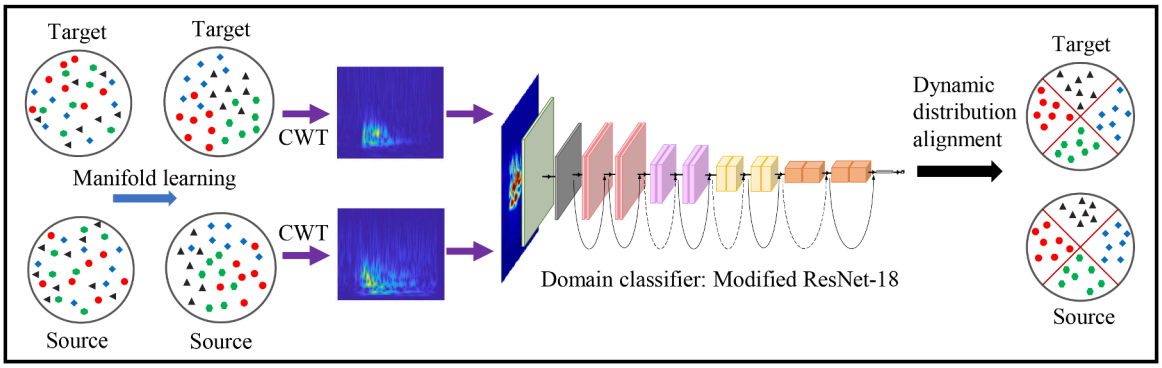

Fig. 8. Flowchart of MEDA-ResNet-18.

mentioned that the data augmentation is unsupervised. No information on labels is used during the process.

4.3. Improved manifold embedded distribution alignment

The original MEDA employs k-nearest neighbor (KNN) as the domain classifier in the dynamic distribution alignment process. The domain classifier can derive labels for the target domain. However, the data in source and target domain in this paper are high-dimensional time series with 2048 sample points, the machine learning model such as KNN does not perform well when dealing with high-dimensional inputs without feature extraction. Previous research has reported that convolutional neural network (CNN) structures such as ResNet, and GoogLeNet work well on the identification of raw acoustic emission signals in applications such as the monitoring of the fracture of stay cable in bridges [56] and the wear of bearings [57,58]. Therefore, an improved MEDA is developed by replacing the KNN classifier with the ResNet-18. This paper names the improved MEDA as MEDA-ResNet-18. The procedures of MEDA-ResNet-18 are presented in Fig. 8.

ResNet-18 is a CNN structure with the idea of residuals [59]. Sometimes, the performance of the network becomes less reliable when using a deeper structure due to gradient vanishing/explosion problems hindering network convergence. A residual block module was developed and applied in the ResNet-18 structure to overcome this problem by introducing skip connections that enable gradients to flow across several layers. The skip connections cause the outputs to learn a residual mapping.

In this paper, the last FC layer of ResNet-18 is modified to have the class number consistent with the number of zones on the steel plate.

The data in the source and target domain after manifold feature learning is converted to continuous wavelet transform (CWT) images and utilized as the input for the ResNet-18 model, because the ResNet-18 network requires RGB images as input. Converting the raw AE signals into time–frequency coefficients and present them by RGB colors can be a good way to prepare the input data for a deep neural network, while retaining most of the useful information. It has been verified to be reliable by previous studies [23,39,60]. This paper used the Morse wavelet as the mother wavelet function to conduct CWT. The Fourier transform of Morse wavelet is presented in Eq. (12):

$$\Psi_{p,\gamma}(x) = U(x)\alpha_{p,\gamma}x^{\frac{p^2}{\gamma}}e^{-x^{\gamma}} \tag{12}$$

where $U(x)$ refers to the unit step, $\alpha_{p,\gamma}$ refers to the normalizing constant, p^2 refers to the time-bandwidth product, γ is the parameter that characterizes the symmetry of the Morse wavelet [61]. In this paper, p^2 and γ were defined as 60 and 3, respectively.

5. Results and discussion

5.1. Experimental recorded acoustic emission waveforms

AE signals were continuously collected during the PLB experiments. Each of the signals is a time series with 2,048 sample points since the sampling rate of the data acquisition was set to 1 MHz, and the duration was set to 2,048 μs. Because the elastic waves are

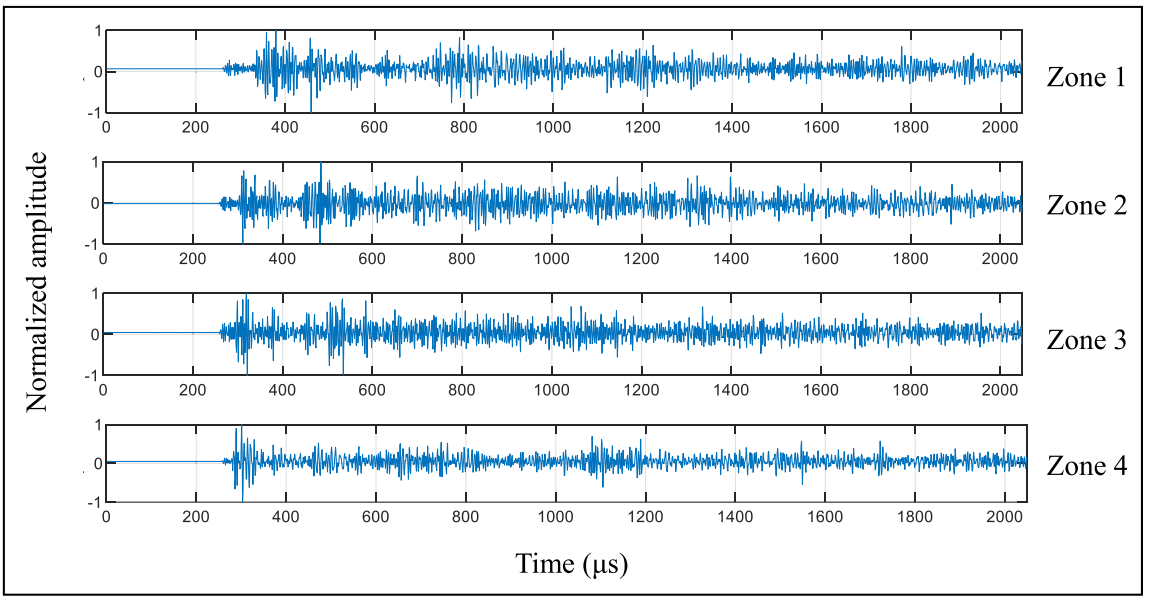

Fig. 9. Waveforms of the normalized AE signals in each zone.

subject to dispersion and attenuation during propagation, the amplitude of the AE signals varies substantially in different zones. If the AE signals are used as the input of a deep learning model without normalization, the model will focus on the amplitude, while other key properties may be overlooked and have a substantial impact on the performance of the model. Therefore, all AE signals were normalized by amplitude to a range of −1 to 1 and utilized as the target domain in this paper. The waveforms of the normalized signals that were randomly selected from each zone are presented in Fig. 9. It can be seen that the patterns of the AE waveforms in different zones are varied. The proposed approach can recognize waveform patterns and classify them into the appropriate zones.

5.2. Numerical acoustic emission waveforms

The results of the finite element modeling are presented in Fig. 10. This figure represents expected wave propagation, in terms of out-of-plane displacement, from the point where the excitation source is applied. The wave generated by excitations in four zones is captured by a sensor and converted to numerical AE waveforms according to the method introduced in Section 4.1. It can be seen that different numerical signals generated from different points are varied, especially the side-reflections in the reverberation signals. These

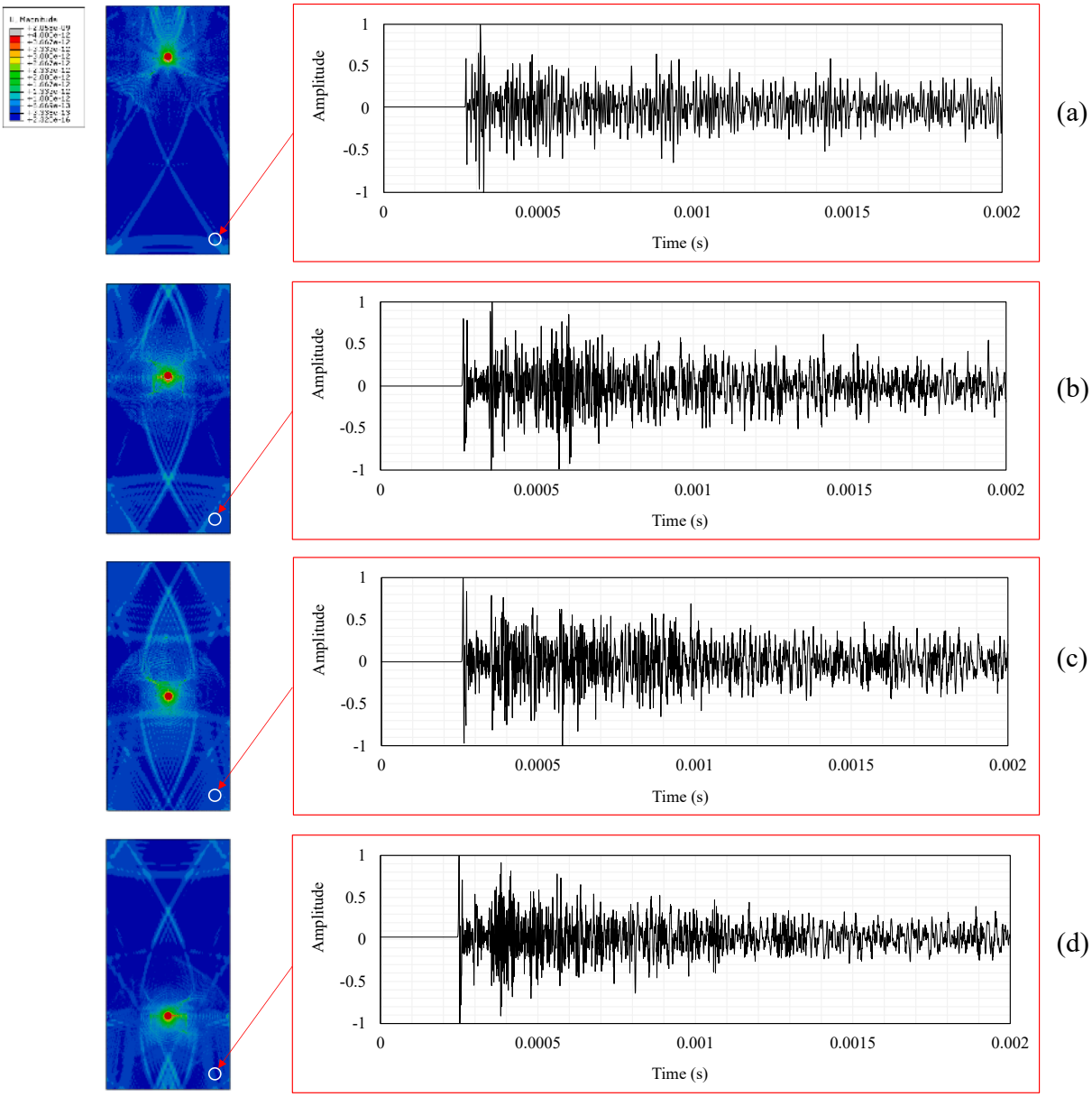

Fig. 10. Results of AE simulation: (a) wave propagated from zone 1; (b) wave propagated from zone 2; (c) wave propagated from zone 3; (d) wave propagated from zone 4.

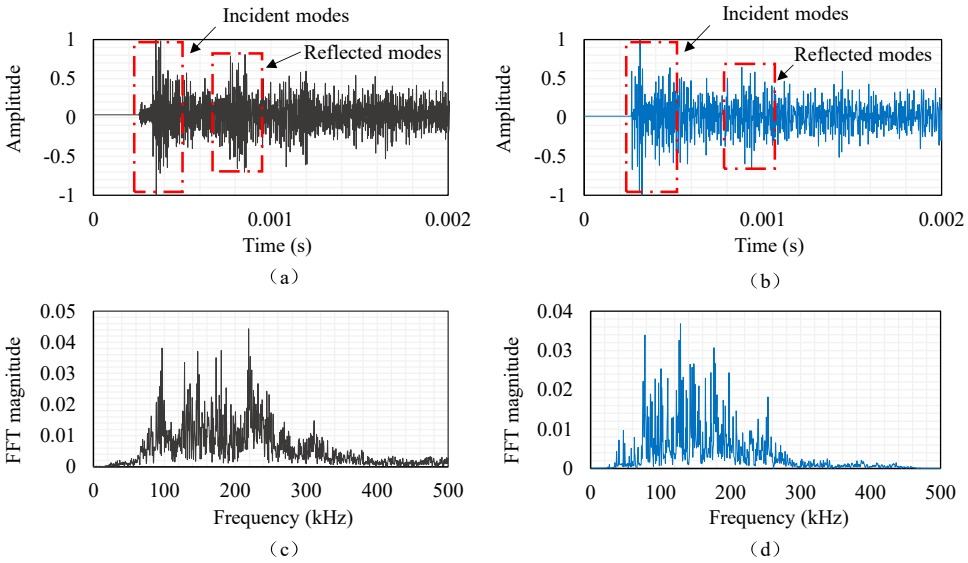

Fig. 11. Experimental signals versus numerical signals: (a) experimental waveform; (b) numerical waveform; (c) experimental FFT spectrum; (d) numerical FFT spectrum.

differences are caused by the position of the PLB and the boundaries of the plate. In the later analysis, the distribution of these numerical signals is dynamically aligned with the distribution of the experimental signals.

When AE signals propagate through imperfections or discontinuities, scattering phenomena such as reflection, transmission, and interference will happen, causing a considerable change in the modes and characteristics of the original signals [62]. It is important to discuss scattering because scattering determines the reverberation patterns of AE signals, and the deep learning classifier (ResNet-18) adopted in this paper learns the reverberation pattern to locate the damage. A typical numerical AE waveform and a typical experimental AE waveform from zone 1 were shown in Fig. 11a and 11b to compare the scattering characteristic. The amplitudes of

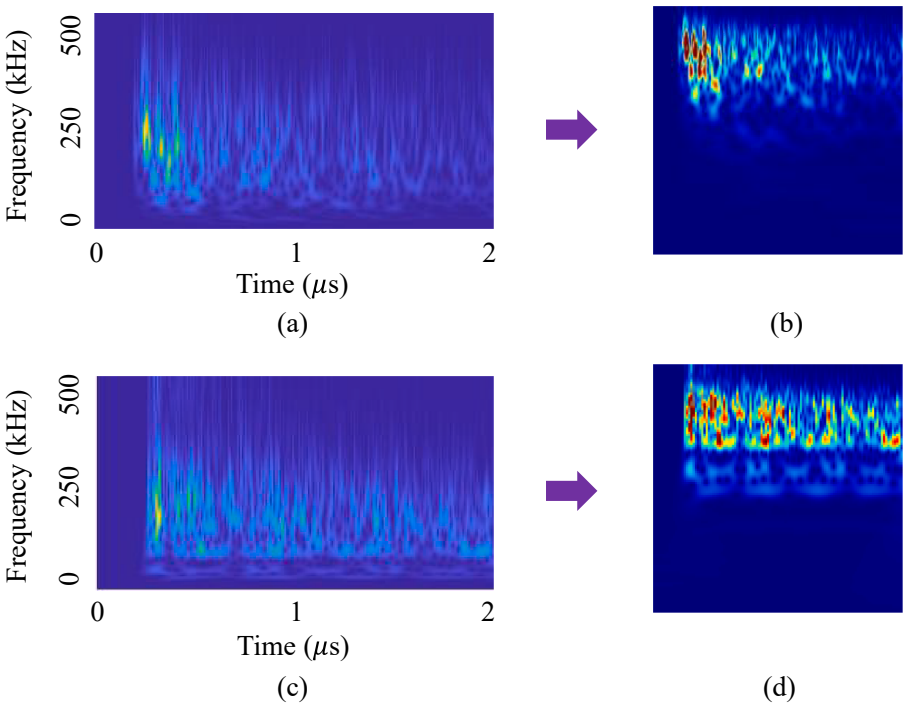

Fig. 12. Continuous wavelets transform of source and target domain: (a) CWT coefficients of source domain; (b) RGB image of source domain; (c) CWT coefficients of the target domain; (d) RGB image of the target domain.

waveforms were normalized from −1 to 1. The incident wave and a major reflected waves are marked with red boxes. Reflection coefficients of the marked major reflection for the numerical and experimental signals were calculated. The reflection coefficient is defined as the amplitude ratio of the reflected signal to the incident signal. It can be calculated by the equation [62] below:

$$RC = \left| U_R^m(z)/U(z) \right| \tag{13}$$

where, RC represents the reflection coefficient, $U(z)$ refers to the amplitude of the incident wave, and $U_R^m(z)$ is the amplitude of the m-th reflected wave. According to the equation, the RC is found to be 0.65 for the numerical signal and 0.78 for the experimental signal. The small difference in RC between the simulated and experimental signals suggests that they have relatively similar reflection characteristics and reverberation patterns. Please note that this paper only discussed the reflection characteristic because the specimen used herein is a simple plate. For the more complex structures in further field application such as steel plates with joints, bolts, and welds, the transmission characteristic should also be studied. Similar to the reflection coefficient, the transmission coefficient can be obtained by Eq. (14) [62]:

$$TC = \left| U_T^m(z)/U(z) \right| \tag{14}$$

where, TC represents the transmission coefficient, $U_T^m(z)$ refers to the amplitude of the transmitted mode.

In addition to compare the waveform and scattering characteristic, the frequency components of the signals can also be significant to investigated. Fast Fourier transformation (FFT) analysis was conducted, with the frequency spectrums shown in Fig. 11c and d. It can be noticed that the primary frequency of the experimental signal is in the range of 100–250 kHz (Fig. 11c). In the numerical FFT magnitude (Fig. 11d), the primary frequency also lies in 100–250 kHz which is aligned with the experimental signal frequency range.

In summary, the numerical and experimental signals have similar reverberation patterns and scattering characteristic in the waveforms. Moreover, there is an alignment of the frequency component between the experimental and numerical signals. Those suggest that the numerical signal can simulate the experimental signal to some extent. However, there are still some differences between the waveforms of the experimental and numerical signals, which indicates that the simulation and the experiment are not completely consistent. The UDA method proposed in this paper (MEDA-ResNet-18) is aimed to address this issue. It could learn the common marginal and conditional distributions between the experimental and the numerical signals and to reduce the differences between them.

5.3. Results of UDA and transfer learning

The 480 numerical AE waveforms after data augmentation are utilized as the source domain and the 400 AE signals recorded by the experiment are used as the target domain. GFK manifold feature learning is utilized to decrease the difference in distribution of the source and target domains. After GFK manifold feature learning, the waveforms in the reconstructed source and target domain are transformed to CWT coefficients. Fig. 12a and c illustrate example CWT coefficients of signals from source and target domain when the dimension of the low-dimensional manifold space is 190. The wavelet coefficients are scaled between 0 and 1. The Y-axis of the CWT coefficient was then converted to a logarithmic coordinate to present the time–frequency component more clearly. The coefficients were saved as RGB images with the size of 224 × 224 × 3 pixels (Fig. 12b and 12d). The RGB images are employed as the input of the ResNet-18 domain classifier.

The CWT images in the source domain are employed to train the CNN model in MEDA-ResNet-18. The training dataset contains 90 % of the randomly selected CWT images in the source domain. A validation dataset is constructed by the remaining 10 % of the CWT images. The computing of the CNN model is conducted on a workstation with a CPU-Intel i7-6700 3.40 GHz, 32 GB RAM, and an Nvidia GPU-GTX1080. For the ResNet-18 deployed in this paper, the gradient descent optimization was conducted using the Adaptive moment estimation (Adam) method [63]. The minibatch size was 32 and the learning rate was 0.0001. Fig. 13a and 13b present the accuracy and loss curves of the training and validation datasets from iteration 1 to 90. Both training and validation datasets approach 100 % accuracy by the end of iteration 90, and the losses are close to 0. The training and validation reach the convergence around

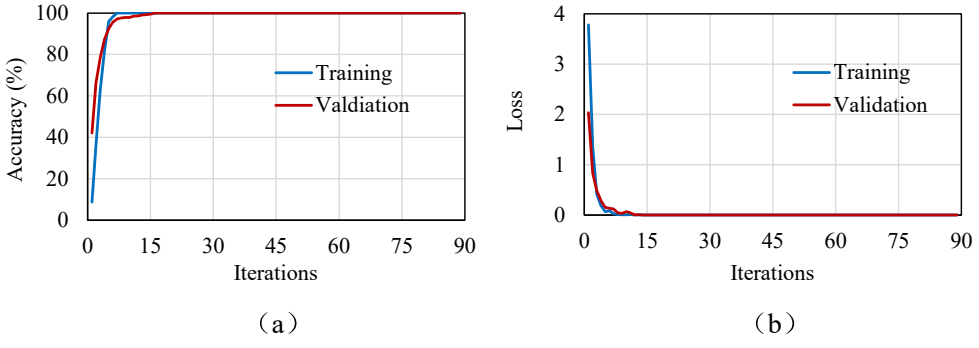

Fig. 13. Training and validation curves: (a) accuracy curves; (b) loss curves.

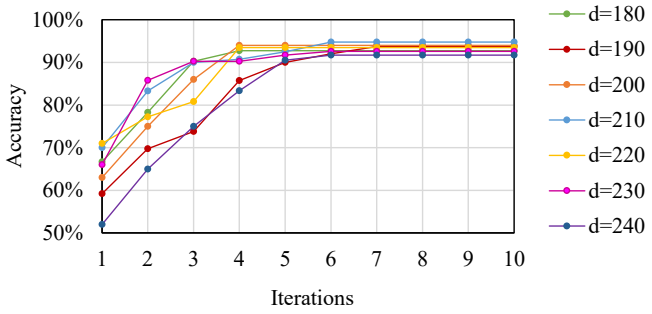

Fig. 14. Iteration of dynamic distribution alignment in MEDA-ResNet-18.

iteration 5, and the curves are stable after converging.

After the ResNet-18 model is trained by the source domain, the CWT images in the target domain are input into the trained model to derive the prediction label. As mentioned in Section 2.2.2, the derived label may not be accurate. The optimized prediction label can be obtained by dynamic distribution alignment after several iterations are conducted. The optimized prediction label is the final output of the MEDA-ResNet-18. In addition to the iteration number, the dimension of the low-dimensional manifold space *d* utilized during the manifold feature learning is another factor that can influence the result of MEDA-ResNet-18. To acquire the appropriate iteration number and dimension of manifold space, a trial-and-error test was conducted with results presented in Fig. 14.

Seven manifold space dimensions (180, 190, 200, 210, 220, 230, and 240) are utilized in MEDA-ResNet-18. For all dimensions, the accuracies of the predicted label increased to over 90 % after iteration 5. The accuracies remain almost constant as the number of iterations increases to 10. This indicates that the iteration number should be at least 5. The highest accuracy (94.8 %) can be observed when the manifold space dimension is 210. Therefore, 210 was selected as the optimum manifold space dimension for MEDA-ResNet-18.

5.4. Comparison and discussion

5.4.1. Discussion of the effectiveness of the proposed TL approach

To evaluate the effectiveness of the proposed TL approach, six scenarios are designed, and their corresponding accuracies are compared. The six scenarios are:

1) Scenario 1: train and test with all the numerical waveforms in the source domain.
2) Scenario 2: train and test with all the experimental waveforms in the target domain.
3) Scenario 3: train on the source domain and test on the target domain without using UDA methods.
4) Scenario 4: train on the source domain and test on the target domain with GFK manifold feature learning, no dynamic distribution alignment is conducted.
5) Scenario 5: train on the source domain and test on the target domain with the original MEDA.

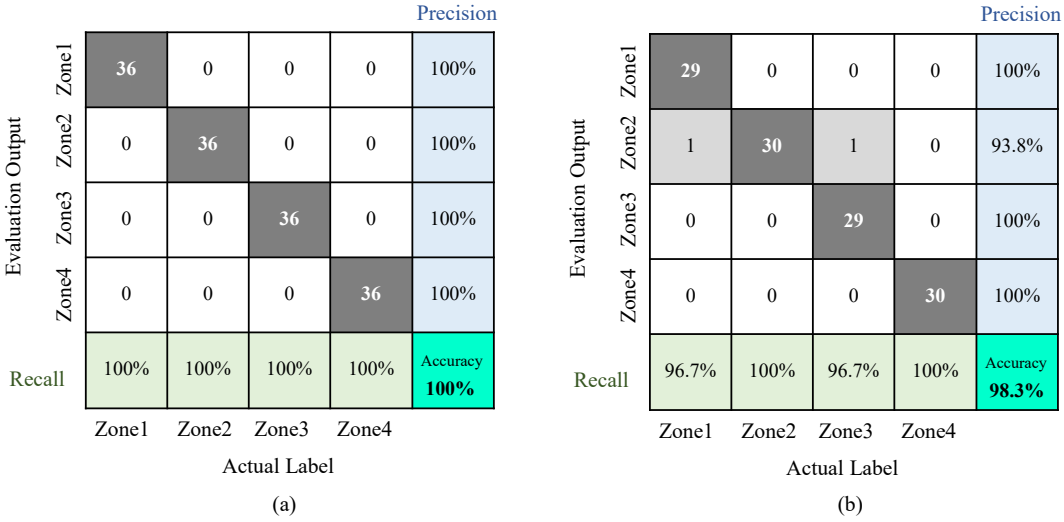

Fig. 15. Source localization accuracy: (a) scenario 1; (b) scenario 2.

6) Scenario 6: train on the source domain and test on the target domain with improved MEDA-ResNet-18.

The goal of scenarios 1 and 2 is to study the performance of AE source localization on the specimen if a sufficient number of well-labeled training data is available. ResNet-18 is employed in the two scenarios. The training, validation, and testing ratio are 80 %, 10 %, and 10 %. The results of scenarios 1 and 2 are shown in the confusion matrixes in Fig. 15. The accuracy is 100 % for training and testing on the 1440 numerical waveforms in the source domain. The accuracy is 98.3 % for the 1200 numerical waveforms in the target domain. Results indicate that a good localization performance may be obtained if labeled training data can be provided.

The objective of scenarios 3 to 6 is to investigate the performance of TL when no labeled training AE waveforms are available. The results are presented in the confusion matrixes in Fig. 16. The numbers of AE data that are correctly localized in their corresponding zones are shown in the main diagonal of the confusion matrix. When using 1440 numerical AE waveforms as the source domain, and using 1200 experimental AE waveforms as target domain, meanwhile no UDA method is applied (scenarios 3), a low prediction accuracy (43.5 %) is observed (Fig. 16a). When using GFK manifold feature learning as the UDA method, the prediction accuracy increases from 43.5 % to 78.7 % (Fig. 16b). The accuracy further increases to 90.9 % (Fig. 16c) when the UDA method is changed to MEDA. Finally, the highest prediction accuracy (94.8 %) can be acquired if the improved MEDA-ResNet-18 is utilized (Fig. 16d). By observing the results of the four scenarios, it can be noticed that the prediction accuracy of the target domain significantly increases if UDA is implemented. Among the three UDA methods, the improved MEDA-ResNet-18 described in this paper has the best performance. The localization accuracies of all the scenarios and their training, validation, and testing data are provided in Table 2.

In addition to accuracy, precision rate and recall rate for each class are usually implemented as the metrics to evaluate the classification performance in each class [64]. The value of precision rate and recall rate is obtained through the following equations:

$$Recall = \frac{TP}{TP + FN} \tag{15}$$

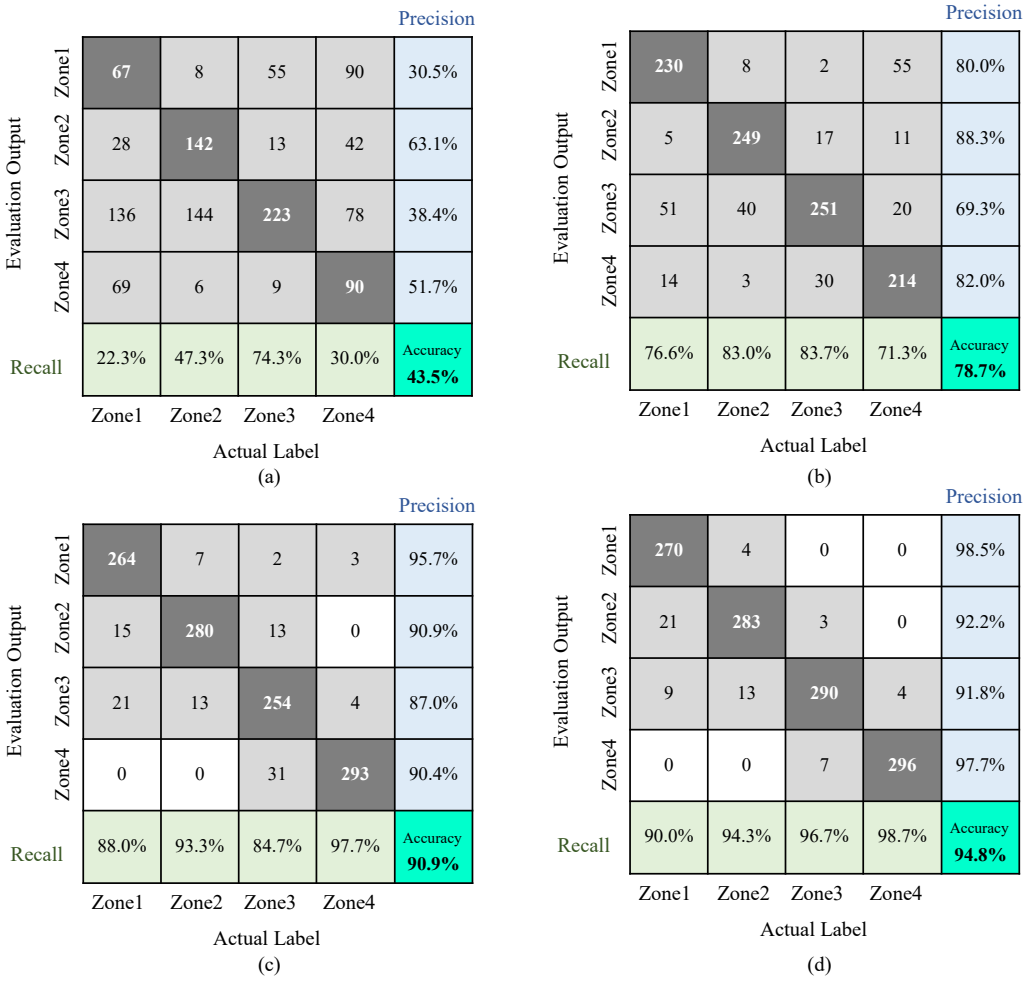

Fig. 16. Source localization accuracy: (a) scenario 3- no UDA; (b) scenario 4- using GFK manifold feature learning; (c) scenario 5- using MEDA; (d) scenario 6- using MEDA-ResNet-18.

Table 2
Accuracies of six scenarios.

Scenarios	Training	Validation	Testing	UDA method	Accuracy
Scenario 1	80 % Source	10 % Source	10 % Source	N/A	100 %
Scenario 2	80 % Target	10 % Target	10 % Target	N/A	98.3 %
Scenario 3	90 % Source	10 % Source	100 %Target	N/A	43.5 %
Scenario 4	90 % Source	10 % Source	100 %Target	GFK	78.7 %
Scenario 5	90 % Source	10 % Source	100 %Target	MEDA	90.9 %
Scenario 6	90 % Source	10 % Source	100 %Target	MEDA-ResNet-18	94.8 %

* Source refers to Numerical AE waveforms; Target refers to Experimental AE waveforms

$$Precision = \frac{TP}{TP + FP} \tag{16}$$

where *TP* refers to true positives, which means the number of samples that correctly classify into the corresponding class, *FP* refers to false positives, which is the number of samples that do not belong to the class but are classified into the class by error, *FN* refers to false negatives, the number of samples that belong to the class but are classified into the other classes by error.

Precision and recall influence each other. A class with high precision usually has a low recall and vice versa [64]. To comprehensively evaluate the efficiency of the classifier in each class, the F1-score can be employed. The F1-score, also referred to as the balanced F score, is defined as the harmonic mean of precision and recall [65]. It can be provided by Eq. (17):

$$F1 = \frac{2 \times Precision \times Recall}{Precision + Recall} = \frac{2TP}{2TP + FP + FN} \tag{17}$$

The comparison of the three metrics, precision rates, recall rates, and F1-score for the four zones of scenarios 3 through 6 are presented in Fig. 17. This figure indicates that the three metrics of scenario 6 using improved MEDA-ResNet-18 are generally the highest, particularly much higher than scenario 3 using no UDA. It can be noticed that the three metrics obtained by scenario 6 are relatively stable, while the other three scenarios show evident variety in different zones. These observations of precision rates, recall rates, and F1-score suggest that scenario 6 using the improved MEDA-ResNet-18 presents the best performance. This is also aligned with the observation of accuracy.

5.4.2. Comparison of the single-sensor source localization methods

The MEDA-ResNet-18 proposed in this paper uses ResNet-18 as a classifier for single-sensor localization. In this section, several single-sensor source localization classifiers for AE, such as artificial neural network (ANN) used in [36], random forest used in [22], GoogLeNet employed in [58], and VGG-19 utilized in [5], were compared and discussed. Those methods were validated using scenario 2 (train and test with all the experimental AE signals). The input data of the ANN and random forest are the parametric features extracted from the AE waveforms. The names of the features and their description are presented in Table 3.

The ANN used in the comparison has 2 layers with 21 neurons each layer. The number of decision trees in the random forest model was set to 200. These hyperparameters were determined after conducting serval trial and error tests. The GoogLeNet, VGG-19, and ResNet-18 were trained and tested on a workstation with a CPU-Intel i7-6700 3.40 GHz, 32 GB RAM, and an Nvidia GPU-GTX1080. The localization accuracies of ANN, random forest, GoogLeNet, VGG-19, and ResNet-18 are presented in Table 4. The highest accuracy (98.5 %) was obtained by ResNet-18. This demonstrates that the performance of the single-sensor source localization method using ResNet-18 is respectable. Applying it to the TL method (MEDA-ResNet-18) proposed in this paper is appropriate.

5.4.3. The influence of the mother wavelets functions

This section compares and discusses the impact of using different mother wavelets functions on the ResNet-18 localization method. Three types of mother wavelets functions: Morse wavelet, Analytic Morlet wavelet, and Bump wavelet were utilized in this comparison. The wavelets images generated by these three kinds of wavelet functions are fed to the ResNet-18 model. The model was validated using scenario 2 (train and test with all the experimental AE signals). The accuracies of using different mother wavelets functions are listed in Table 5.

The results showed that using different mother functions has a minor effect on the performance of the model. Among them, the images generated by Morse and Morlet can yield slightly higher accuracies than Bump. This paper selected Morse wavelets function as the mother function in this paper.

5.4.4. The influence of the size of the target domain

In the field application, the amount of AE signals from damages on the structures being monitored would be limited. In other words, the size of the target domain would be limited. To investigate the influence brought by the size of the target domain, eight subsets of the target domain were created: (1) subset with 1200 samples; (2) subset with 900 samples; (3) subset with 600 samples; (4) subset with 300 samples; (5) subset with 240 samples; (6) subset with 180 samples; (7) subset with 120 samples; (8) subset with 60 samples. The accuracy of the proposed TL approach using the above eight subsets as the target domains is presented in Fig. 18. It can be observed, that as the number of signals in the target domain gets smaller, there is a decrease in the accuracy of localization. The decrease in accuracy is not significant as the number of signals decreases from 1200 to 300, only dropping from 94.8 % to 91.0 %. When there are

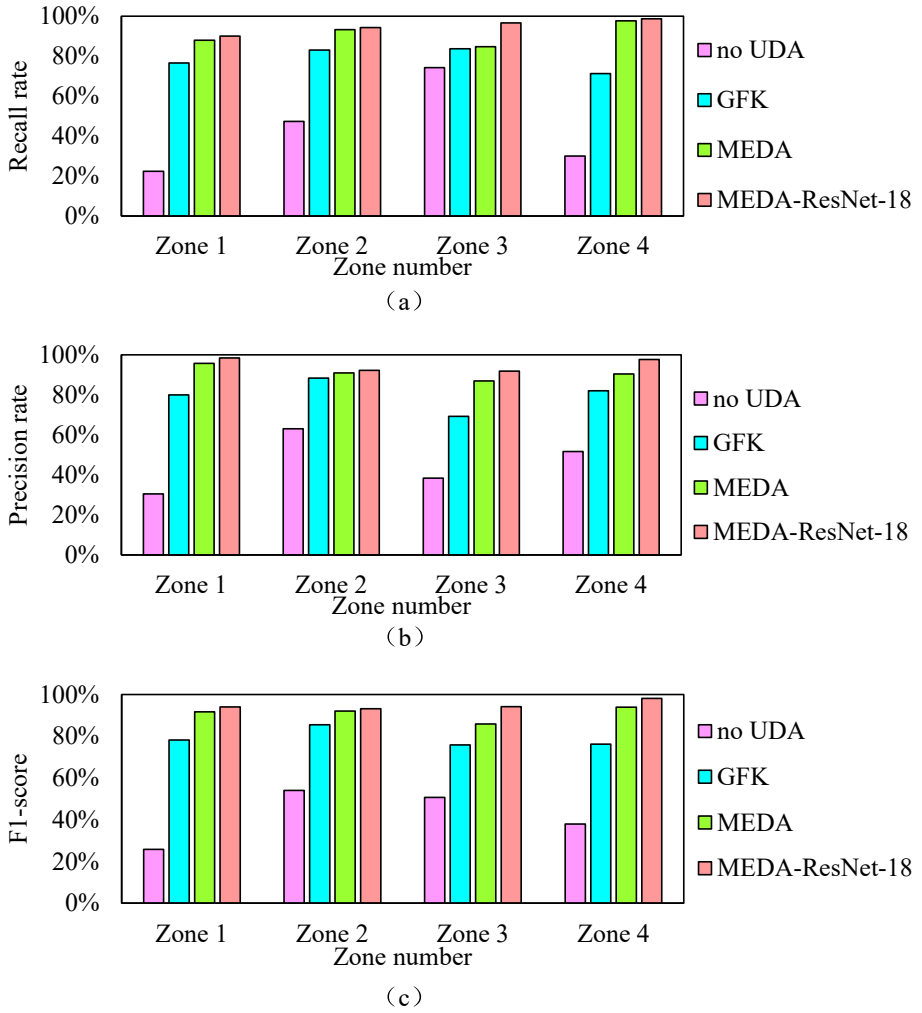

Fig. 17. Comparison of classification performance in each zone: (a) recall rate; (b) precision rate; (c) F1-score.

Table 3
Descriptions of the input parametric features.

Parametric features	Feature descriptions
Amplitude	The peak amplitude of AE waveform
Energy	The measure of the electrical energy measured for an AE signal
Count	The number of threshold crossings
Counts to peak (PCNTS)	The number of threshold crossings from the first threshold crossing to the peak
Rise time	The time interval between first threshold crossing and peak
Duration	The time between the first and last threshold crossing
Average frequency	Counts divided by Duration
Signal strength	A parameter to characterize the overall frequency content of an AE signal
Absolute energy	The absolute measure of the electrical energy measured for an AE signal
Peak frequency	Frequency of maximum signal contribution
Reverberation frequency	Frequency after the peak
Initial frequency	Frequency before the peak
Signal strength	Integral of the rectified voltage signal over the duration of the AE waveform

240 signals in the target domain, the accuracy is 87.5 %, which is an acceptable result. However, if the number of signals continues to drop, a significant decrease in accuracy is observed. When there are 60 signals left in the target domain, the accuracy of localization is 55 %. This illustrates that the TL approach proposed in the present paper has requirements on the number of signals in the target domain. To obtain acceptable source location results, the number of signals in the target domain needs to reach 16.7 % (240signals / 1440signals) of the number of signals in the source domain.

Table 4
Accuracies of different single-sensor source localization methods.

Models	Accuracy
ANN	91.7 %
Random forest	94.1 %
GoogLeNet	96.7 %
VGG-19	96.7 %
ResNet-18	98.3 %

Table 5
Accuracy of ResNet-18 using different wavelets functions.

Input	Accuracy
Input: CWT-Morse	98.3 %
Input: CWT-Morlet	98.3 %
Input: CWT-Bump	97.5 %

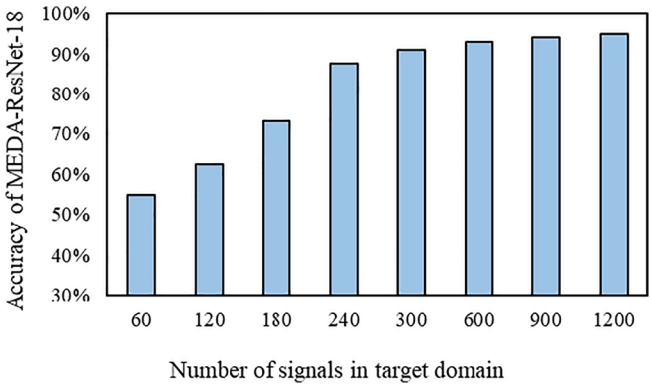

Fig. 18. Influence of the number of AE signals in the target domain.

6. Summary and conclusions

The Supervised learning algorithms have been investigated to localize AE signals on metallic structures [22]. However, the difficulty of accessing the labeled AE signals is a crucial challenge. This paper proposes a TL approach for the localization of acoustic emission on metallic structures without historical AE signals for training. A finite element model is developed to simulate stress wave propagation and generate numerical AE signals. The distribution difference of the numerical and realistic AE signals is reduced by an improved MEDA-ResNet-18 UDA method, and the source localization results of the realistic AE signals are acquired. To evaluate the effectiveness of the proposed approach on metallic structures, a 304 stainless steel plate was used as an experimental specimen to collect AE signals and validate the proposed approach. The main conclusions of the paper are summarized as follows:

The performance of source localization approach using the ResNet-18 model is studied by respectively using the collected experimental AE signals and numerical signals. Results indicate that a good localization performance can be observed when the labeled training data is available.

The numerical signals generated by the finite element model are employed as the labeled source domain. The experimental AE signals are adopted as the unlabeled target domain. The TL source localization accuracies of the scenarios not employing the UDA method (43.5 %), using the GFK method (78.7 %), using MEDA (90.9 %), and using the improved MEDA-ResNet-18 (94.8 %) are compared and discussed. The results suggest that using the UDA method can significantly increase the localization accuracy on the target domain. The best performance was obtained by the improved MEDA-ResNet-18 (94.8 %). Recall rate, precision rate, and F1-score suggest that the improved MEDA-ResNet-18 has the optimum performance of localization for each individual zone.

The frequency content of the signal generated by the finite element model is similar to the values attributed to the experimental AE signal. However, the similarity between the waveforms of the numerical and experimental AE signal is not significant. Future work can focus on improvement of the model by developing a surface output that is more realistic than the single line output adopted in this paper. Another recommendation for future work could be to place more points in each zone so that deep learning models can learn the signature of signals at different locations in the region. This could make the zonal source localization approach more reliable and stable.

The limitation of the current study is that the proposed method was developed based on a simple steel plate. Future work and the

effort may be needed to apply the method on more complex structures (e.g., plates with joints, bolts, and welds) to further extend the reliability and stability of our proposed method.

Declaration of Competing Interest

The authors declare that they have no known competing financial interests or personal relationships that could have appeared to influence the work reported in this paper.

Data availability

Data will be made available on request.

Acknowledgment

This research was partially supported by Electric Power Research Institute (EPRI) under project number 1-108781, and the U.S Department of Energy-Nuclear Energy University Program (NEUP) under the contract DE-NE0008544. The views and opinions of authors expressed herein do not necessarily state or reflect the opinions of the funding agencies.

References

[1] Y. Zhao, F. Zhou, J. Yao, S. Dong, N. Li, Erosion–corrosion behavior and corrosion resistance of AISI 316 stainless steel in flow jet impingement, Wear 328 (2015) 464–474, https://doi.org/10.1016/j.wear.2015.03.017.
[2] X. Tan, L. Fan, Y. Huang, T. Bao, Detection, visualization, quantification, and warning of pipe corrosion using distributed fiber optic sensors, Autom. Constr. 132 (2021), 103953, https://doi.org/10.1016/j.autcon.2021.103953.
[3] L. Fan, X. Tan, Q. Zhang, W. Meng, G. Chen, Y. Bao, Monitoring corrosion of steel bars in reinforced concrete based on helix strains measured from a distributed fiber optic sensor, Eng. Struct. 204 (2020), 110039, https://doi.org/10.1016/j.engstruct.2019.110039.
[4] D. Aggelis, E. Kordatos, T. Matikas, Acoustic emission for fatigue damage characterization in metal plates, Mech. Res. Commun. 38 (2011) 106–110, https://doi.org/10.1016/j.mechrescom.2011.01.011.
[5] L. Ai, V. Soltangharaei, P. Ziehl, Evaluation of ASR in concrete using acoustic emission and deep learning, Nucl. Eng. Des. 380 (2021), 111328, https://doi.org/10.1016/j.nucengdes.2021.111328.
[6] M.R. Pearson, M. Eaton, C. Featherston, R. Pullin, K. Holford, Improved acoustic emission source location during fatigue and impact events in metallic and composite structures, Struct. Health Monit. 16 (2017) 382–399, https://doi.org/10.1177/1475921716672220.
[7] Y. Sai, M. Jiang, Q. Sui, S. Lu, L. Jia, Multi-source acoustic emission localization technology research based on FBG sensing network and time reversal focusing imaging, Optik 127 (2016) 493–498, https://doi.org/10.1016/j.ijleo.2015.09.067.
[8] Y. Yan, Y. Shen, X. Cui, Y. Hu, Localization of multiple leak sources using acoustic emission sensors based on MUSIC algorithm and wavelet packet analysis, IEEE Sens. J. 18 (2018) 9812–9820, https://doi.org/10.1109/JSEN.2018.2871720.
[9] M.I. Jordan, T.M. Mitchell, Machine learning: Trends, perspectives, and prospects, Science 349 (2015) 255–260, https://doi.org/10.1126/science.aaa8415.
[10] I. Goodfellow, Y. Bengio, A. Courville, Machine learning basics, Deep Learn. 1 (2016) 98–164.
[11] V. Cherkassky, Y. Ma, Practical selection of SVM parameters and noise estimation for SVM regression, Neural Netw. 17 (2004) 113–126, https://doi.org/10.1016/S0893-6080(03)00169-2.
[12] L. Ai, V. Soltangharaei, R. Anay, M.J. van Tooren, P. Ziehl, Data-Driven Source Localization of Impact on Aircraft Control Surfaces, IEEE 1–10 (2020), https://doi.org/10.1109/AERO47225.2020.9172742.
[13] L. Ai, V. Soltangharaei, P. Ziehl, Developing a heterogeneous ensemble learning framework to evaluate Alkali-silica reaction damage in concrete using acoustic emission signals, Mech. Syst. Sig. Process. 172 (2022), 108981, https://doi.org/10.1016/j.ymssp.2022.108981.
[14] K. Laxman, A. Ross, L. Ai, A. Henderson, E. Elbatanouny, M. Bayat, P. Ziehl, Determination of vehicle loads on bridges by acoustic emission and an improved ensemble artificial neural network, Constr. Build. Mater. 364 (2023), 129844, https://doi.org/10.1016/j.conbuildmat.2022.129844.
[15] I. Goodfellow, Y. Bengio, A. Courville, Y. Bengio, Deep learning, MIT Press Cambridge, 2016.
[16] S. Laflamme, C. Hu, J. Dodson, in, Structural Health Monitoring Based on Data Science Techniques, Springer, 2022, pp. 75-94. https://doi.org/10.1007/978-3-030-81716-9_4.
[17] V. Ewald, R.S. Venkat, A. Asokkumar, R. Benedictus, C. Boller, R.M. Groves, Perception modelling by invariant representation of deep learning for automated structural diagnostic in aircraft maintenance: A study case using DeepSHM, Mech. Syst. Sig. Process. 165 (2022), 108153, https://doi.org/10.1016/j.ymssp.2021.108153.
[18] V. Barzegar, S. Laflamme, C. Hu, J. Dodson, Ensemble of recurrent neural networks with long short-term memory cells for high-rate structural health monitoring, Mech. Syst. Sig. Process. 164 (2022), 108201, https://doi.org/10.1016/j.ymssp.2021.108201.
[19] A. Ebrahimkhanlou, S. Salamone, Acoustic emission source localization in thin metallic plates: A single-sensor approach based on multimodal edge reflections, Ultrasonics 78 (2017) 134–145, https://doi.org/10.1016/j.ultras.2017.03.006.
[20] A. Ebrahimkhanlou, S. Salamone, A probabilistic framework for single-sensor acoustic emission source localization in thin metallic plates, Smart Mater. Struct. 26 (9) (2017) 095026.
[21] A. Ebrahimkhanlou, B. Dubuc, S. Salamone, A generalizable deep learning framework for localizing and characterizing acoustic emission sources in riveted metallic panels, Mech. Syst. Sig. Process. 130 (2019) 248–272, https://doi.org/10.1016/j.ymssp.2019.04.050.
[22] L. Ai, V. Soltangharaei, M. Bayat, B. Greer, P. Ziehl, Source localization on large-scale canisters for used nuclear fuel storage using optimal number of acoustic emission sensors, Nucl. Eng. Des. 375 (2021), 111097, https://doi.org/10.1016/j.nucengdes.2021.111097.
[23] C. Han, T. Liu, Y. Jin, G. Yang, Acoustic Emission Intelligent Identification for Initial Damage of the Engine based on Single Sensor, Mech. Syst. Sig. Process. 169 (2022), 108789, https://doi.org/10.1016/j.ymssp.2021.108789.
[24] S.J. Pan, Q. Yang, A survey on transfer learning, IEEE Trans. Knowl. Data Eng. 22 (2009) 1345–1359, https://doi.org/10.1109/TKDE.2009.191.
[25] D. Li, Y. Wang, W.-J. Yan, W.-X. Ren, Acoustic emission wave classification for rail crack monitoring based on synchrosqueezed wavelet transform and multi-branch convolutional neural network, Struct. Health Monit. 20 (4) (2021) 1563–1582.
[26] S.-X. Chen, L.u. Zhou, Y.-Q. Ni, X.-Z. Liu, An acoustic-homologous transfer learning approach for acoustic emission–based rail condition evaluation, Struct. Health Monit. 20 (4) (2021) 2161–2181.
[27] M. Long, H. Zhu, J. Wang, M.I. Jordan, 2016. Unsupervised domain adaptation with residual transfer networks, arXiv preprint arXiv:1602.04433.
[28] J. Wang, W. Feng, Y. Chen, H. Yu, M. Huang, P.S. Yu, 2018, Visual domain adaptation with manifold embedded distribution alignment, 402-410. https://doi.org/10.1145/3240508.3240512.
[29] Z. Zhang, J. Wang, H. Zha, Adaptive manifold learning, IEEE Trans. Pattern Anal. Mach. Intell. 34 (2011) 253–265, https://doi.org/10.1109/TPAMI.2011.115.

[30] B. Gong, Y. Shi, F. Sha, K. Grauman, Geodesic flow kernel for unsupervised domain adaptation, IEEE 2066–2073 (2012), https://doi.org/10.1109/CVPR.2012.6247911.
[31] M. Arbel, A. Korba, A. Salim, A. Gretton, Maximum mean discrepancy gradient flow, Adv. Neural Inf. Proces. Syst. 2019 (2019) 32.
[32] B. Quanz, J. Huan, Large margin transductive transfer learning, 1327–1336, in: Proceedings of the 18th ACM Conference on Information and Knowledge Management, 2009, https://doi.org/10.1145/1645953.1646121.
[33] S. Ben-David, J. Blitzer, K. Crammer, F. Pereira, Analysis of representations for domain adaptation, Adv. Neural Inf. Proces. Syst. 19 (2007) 137.
[34] C. Grosse, M. Ohtsu (Eds.), Acoustic Emission Testing, Springer Berlin Heidelberg, Berlin, Heidelberg, 2008.
[35] V. Soltangharaei, R. Anay, L. Ai, E.R. Giannini, J. Zhu, P. Ziehl, Temporal evaluation of ASR cracking in concrete specimens using acoustic emission, J. Mater. Civ. Eng. 32 (2020) 04020285, https://doi.org/10.1061/(ASCE)MT.1943-5533.0003353.
[36] L. Ai, V. Soltangharaei, M. Bayat, M. van Tooren, P. Ziehl, 2021. Detection of impact on aircraft composite structure using machine learning techniques, Meas. Sci. Technol., 32, 084013. https://doi.org/10.1088/1361-6501/abe790.
[37] T. Boczar, M. Lorenc, Determining the repeatability of acoustic emission generated by the Hsu-Nielsen calibrating source, Molecular Quantum Acoustics 25 (2004) 177–192.
[38] A. Jierula, S. Wang, T.-M. Oh, J.-W. Lee, J.H. Lee, Detection of source locations in RC columns using machine learning with acoustic emission data, Eng. Struct. 246 (2021), 112992, https://doi.org/10.1016/j.engstruct.2021.112992.
[39] S. Sikdar, D. Liu, A. Kundu, Acoustic emission data based deep learning approach for classification and detection of damage-sources in a composite panel, Compos. B Eng. 228 (2022), 109450, https://doi.org/10.1016/j.compositesb.2021.109450.
[40] L. Yang, F. Xu, A novel acoustic emission sources localization and identification method in metallic plates based on stacked denoising autoencoders, IEEE Access 8 (2020) 141123–141142, https://doi.org/10.1109/ACCESS.2020.3012521.
[41] D.F. Hesser, S. Mostafavi, G.K. Kocur, B. Markert, Identification of acoustic emission sources for structural health monitoring applications based on convolutional neural networks and deep transfer learning, Neurocomputing 453 (2021) 1–12, https://doi.org/10.1016/j.neucom.2021.04.108.
[42] B. Hosten, M. Castaings, Finite elements methods for modeling the guided waves propagation in structures with weak interfaces, J. Acoust. Soc. Am. 117 (2005) 1108–1113, https://doi.org/10.1121/1.1841731.
[43] E.H. Saenger, N. Gold, S.A. Shapiro, Modeling the propagation of elastic waves using a modified finite-difference grid, Wave Motion 31 (2000) 77–92, https://doi.org/10.1016/S0165-2125(99)00023-2.
[44] M.G. Sause, S. Richler, Finite element modelling of cracks as acoustic emission sources, J. Nondestr. Eval. 34 (2015) 4.
[45] M.G. Sause, M.A. Hamstad, S. Horn, Finite element modeling of conical acoustic emission sensors and corresponding experiments, Sens. Actuators, A 184 (2012) 64–71, https://doi.org/10.1007/s10921-015-0278-8.
[46] L. Ai, B. Greer, J. Hill, V. Soltangharaei, R.A.P. Ziehl, 2019, Finite element modeling of acoustic emission in dry cask storage systems generated by cosine bell sources, AIP Publishing LLC, 130001. https://doi.org/10.1063/1.5099851.
[47] A.-M. Zelenyak, M.A. Hamstad, M.G. Sause, Modeling of acoustic emission signal propagation in waveguides, Sensors 15 (2015) 11805–11822, https://doi.org/10.3390/s150511805.
[48] N. van Rijn, 2017. Investigating the Behaviour of Acoustic Emission Waves Near Cracks: Using the Finite Element Method.
[49] J.A. Cuadra, A Computational Modeling Approach of Fracture-Induced Acoustic Emission, Drexel University, 2015.
[50] J.A. Cuadra, P. Vanniamparambil, D. Servansky, I. Bartoli, A. Kontsos, Acoustic emission source modeling using a data-driven approach, J. Sound Vib. 341 (2015) 222–236, https://doi.org/10.1016/j.jsv.2014.12.021.
[51] I.W. Selesnick, C.S. Burrus, Generalized digital Butterworth filter design, IEEE Trans. Signal Process. 46 (1998) 1688–1694, https://doi.org/10.1109/78.678493.
[52] D.G.E. Robertson, J.J. Dowling, Design and responses of Butterworth and critically damped digital filters, J. Electromyogr. Kinesiol. 13 (2003) 569–573, https://doi.org/10.1016/S1050-6411(03)00080-4.
[53] M. Shehadeh, A. Elbatran, A. Mehanna, J. Steel, R. Reuben, Evaluation of acoustic emission source location in long steel pipes for continuous and semi-continuous sources, J. Nondestr. Eval. 38 (2019) 1–15, https://doi.org/10.1007/s10921-019-0577-6.
[54] Y. Kurokawa, Y. Mizutani, M. Mayuzumi, Frequency filtering algorithms of plate wave AE for source location, Progr. Acoustic Emission 13 (2006) 231.
[55] S. Shinde, G. Yeole, V. Rajput, D. Mehta, Wavelet-Based Denoising of Acoustic Signal, Int. J. Res. Eng. Technol. 3 (2014).
[56] H. Xin, L. Cheng, R. Diender, M. Veljkovic, Fracture acoustic emission signals identification of stay cables in bridge engineering application using deep transfer learning and wavelet analysis, Adv. Bridge Eng. 1 (2020) 1–16, https://doi.org/10.1186/s43251-020-00006-7.
[57] F. König, G. Jacobs, A. Stratmann, D. Cornel, Fault detection for sliding bearings using acoustic emission signals and machine learning methods, IOP Publishing 1097 (1) (2021) 012013.
[58] F. König, C. Sous, A.O. Chaib, G. Jacobs, Machine learning based anomaly detection and classification of acoustic emission events for wear monitoring in sliding bearing systems, Tribol. Int. 155 (2021), 106811, https://doi.org/10.1016/j.triboint.2020.106811.
[59] K. He, X. Zhang, S. Ren, Deep residual learning for image recognition, J. Sun (2016) 770–778.
[60] D. Li, Y. Wang, W.-J. Yan, W.-X. Ren, Acoustic emission wave classification for rail crack monitoring based on synchrosqueezed wavelet transform and multi-branch convolutional neural network, Struct. Health Monit. 20 (2021) 1563–1582, https://doi.org/10.1177/1475921720922797.
[61] J.M. Lilly, S.C. Olhede, Generalized Morse wavelets as a superfamily of analytic wavelets, IEEE Trans. Signal Process. 60 (2012) 6036–6041, https://doi.org/10.1109/TSP.2012.2210890.
[62] C. Han, G. Yang, J. Wang, X. Guo, The research on propagation characteristics of acoustic emission signals in stiffened plates based on the multipath propagation model, Ultrasonics 108 (2020), 106177, https://doi.org/10.1016/j.ultras.2020.106177.
[63] D.P. Kingma, J. Ba, 2014. Adam: A method for stochastic optimization, arXiv preprint arXiv:1412.6980. https://doi.org/10.48550/arXiv.1412.698.
[64] M. Buckland, F. Gey, The relationship between recall and precision, J. Am. Soc. Inf. Sci. 45 (1994) 12–19, https://doi.org/10.1002/(SICI)1097-4571(199401)45:1<12::AID-ASI2>3.0.CO;2-L.
[65] H. Huang, H. Xu, X. Wang, W. Silamu, Maximum F1-score discriminative training criterion for automatic mispronunciation detection, IEEE/ACM Trans. Audio Speech Lang. Process. 23 (2015) 787–797, https://doi.org/10.1109/TASLP.2015.2409733.